Advanced Functional Materials

ADVANCED FUNCTIONAL MATERIALS
www.afm-journal.de

RESEARCH ARTICLE OPEN ACCESS

Tailoring K^+/Vacancy Disordered Layered Oxide via Charge Engineering for Stabilizing High-Performance Potassium-Ion Batteries

Yongfeng Jia[1] | Xuanpeng Wang[2,3] | Jiashen Meng[3,4] | Lujun Zhu[1] | Fanjie Xia[4] | Hong Wang[4] | Fang Liu[4] | Xiao Zhang[3,5] | Quanquan Pang[1] | Jian Wang[6,7] | Zhitong Xiao[1,4]

[1]School of Materials Science and Engineering, Peking University, Beijing, China | [2]Hubei Longzhong Laboratory, Wuhan University of Technology (Xiangyang Demonstration Zone), Xiangyang, Hubei, China | [3]Zhongyu Feima New Material Technology Innovation Center (Zhengzhou) Co., Ltd. High Technology Industrial Development Zone, Zhengzhou, Henan, China | [4]School of Materials Science and Engineering, State Key Laboratory of Advanced Technology for Materials Synthesis and Processing, Wuhan University of Technology, Wuhan, China | [5]School of Materials Science and Engineering, Zhengzhou University, Zhengzhou, China | [6]Helmholtz Institute Ulm, Ulm, Germany | [7]Karlsruhe Institute of Technology (KIT), Karlsruhe, Germany

Correspondence: Xuanpeng Wang (wxp122525691@whut.edu.cn) | Jian Wang (jian.wang@kit.edu; wangjian2014@sinano.ac.cn) | Zhitong Xiao (xiaozhitong@pku.edu.cn)

Received: 19 January 2026 | **Revised:** 4 February 2026 | **Accepted:** 5 February 2026

Keywords: charge-ion coupling engineering | fast transport kinetics | K^+/vacancy disorder | potassium-ion batteries | single-phase solid-solution mechanism

ABSTRACT

Layered transition metal oxides represent attractive cathode candidates for potassium-ion batteries (PIBs), due to their high theoretical specific capacity. However, sluggish K^+ diffusion and structural instability, stemming from the inherent K^+/vacancy ordered structure, lead to poor rate performance and cycling stability. Herein, a charge-ion coupling engineering strategy, wherein transition-metal electronic structure is tuned to modulate interlayer K^+/vacancy configurations, is initially pioneered. Specifically, a K^+/vacancy-disordered P3-type structure is constructed via targeted transition metal (TM) doping in Mn/Co-based layered oxides. Exploiting the identical valence of Ti^{4+} and Mn^{4+} coupled with their divergent redox potential, the doping sites suppress charge ordering within TM slabs through modulating charge delocalization, thereby inducing interlayer K^+/vacancy disordering. The K^+/vacancy disordered $K_{0.5}Mn_{0.8}Co_{0.1}Ti_{0.1}O_2$ delivers long-term stability with 58.6 mAh g^{-1} over 800 cycles at 1 A g^{-1} and remarkable rate capability of 61.7 mAh g^{-1} at 2 A g^{-1}, facilitating a highly reversible single-phase solid-solution reaction in $K_{0.5}Mn_{0.8}Co_{0.1}Ti_{0.1}O_2$ and enhancing the structural stability during K^+ extraction/insertion. Meanwhile, molecular dynamics simulations demonstrate that the K^+/vacancy disordered structure contains interconnected channels enabling continuous and rapid K^+ diffusion. This work establishes a cation substitution strategy for manipulating K^+/vacancy order-disorder to develop high-performance, kinetically robust cathode materials for next-generation PIBs.

1 | Introduction

Potassium-ion batteries (PIBs) have emerged as promising next-generation energy storage systems owing to the geological abundance of potassium and the favorable redox potential of K^+/K (−2.936 V vs. Standard Hydrogen Electrode) [1–4]. However, cathode development in PIBs still lags behind that of other secondary battery technologies, largely due to the stringent structural constraints imposed by the large ionic radius of K^+ (1.38 Å) [5–8]. Among various candidates, layered transition metal oxides (K_xTMO_2; TM = Mn, Co, Ni, Fe, etc., or their combinations) stand out, offering competitive theoretical specific

capacities, suitable operating voltage, and facile synthesis routes [9–11]. Nevertheless, current implementations suffer from low ion diffusion coefficients and irreversible phase transformations, resulting in poor rate capability and rapid capacity fading, thereby calling for innovative structural engineering strategies to realize their full potential [12, 13].

Due to its large ionic radius, K^+ cannot fully occupy interlayer sites in layered transition metal oxides, resulting in intrinsic K^+ vacancies [14, 15]. Two structural archetypes arise depending on spatial distribution: K^+/vacancy ordered configurations with periodic atomic arrangements and K^+/vacancy disordered structures with stochastic site occupancy. The K^+/vacancy ordered architectures manifest electrochemically as discrete voltage plateaus during K^+ de-intercalation/intercalation and multiple redox peaks in cyclic voltammetry (CV), indicative of stepwise phase transitions [16, 17]. This phenomenon has been widely documented in compounds, such as $K_{0.5}MnO_2$ [17], $K_{0.4}Li_{0.1}Fe_{0.1}Mn_{0.8}O_2$ [18], $K_{0.67}Mn_{0.75}Ni_{0.23}Nb_{0.02}O_2$ [19] and $K_{1/2}Mn_{5/6}Mg_{1/12}Ni_{1/12}O_2$ [20]. Although these features are commonly attributed to K^+/vacancy ordering, their mechanistic origins remain underexplored and unclear. Thermodynamically, K^+/vacancy ordering can stabilize low-energy intermediate superstructures; consequently, K (de)intercalation proceeds through successive first-order transitions with two-phase coexistence, which manifests as staircase-like voltage plateaus and multiple CV redox peaks. Mechanistically, structural rearrangement of the ordered structures during K^+ extraction/insertion induces irreversible phase transformations that progressively degrade the host layered framework [21]. Moreover, the ordered configuration elevates local migration barriers through site-specific energy redistribution, impeding ionic transport kinetics [22, 23]. Strategic disruption of these ordering arrangements to establish K^+/vacancy disordered structure offers a promising route to enhance structural resilience and kinetic performance.

Layered transition metal oxides display two interrelated order-disorder phenomena: (i) Transition metal (TM) charge ordering-disordering, governed by redox potential differences among TM ions—large disparities promote charge localization, whereas small differences stabilize ordered configurations [24]. (ii) Interlayer K^+/vacancy ordering-disordering, which evolves through the coupling of intralayer electrostatic repulsion—determined by K^+ stoichiometry and spatial occupancy—and TM charge ordering-disordering, as electronic correlations reshape the K^+ site-energy landscape [25, 26]. Notably, TM charge ordering imposes crystallographic symmetry that templates K^+/vacancy periodicity, while TM charge disordering reduces interlayer electrostatic anisotropy, favoring randomized K^+/vacancy distributions [27]. Strategic engineering of order-disorder transitions can be achieved primarily through two approaches (Figure 1): (a) Precise stoichiometric control of K^+ content to disrupt long-range electrostatic correlations and drive topological reconstruction toward disordered phases [28]; (b) Targeted TM doping to introduce redox-mismatched pairs, thereby destabilizing charge order and indirectly inducing K^+/vacancy disorder through electronic structure modulation [27]. These two approaches constitute mechanistically distinct yet coupled pathways: (i) a stoichiometry-tuning route (via K-content control) and (ii) a charge-ion coupling regulation route (via TM electronic-structure and charge order modulation). Our systematic stoichiometric engineering of potassium content in manganese-nickel layered oxides ($K_xMn_{0.7}Ni_{0.3}O_2$, $0.4 \leq x \leq 0.7$) achieves controllable order-disorder transitions in K^+/vacancy configurations, with progressive potassium enrichment driving a continuous structural evolution from ordering to disordering [28]. Electrochemical evaluation reveals that the K^+/vacancy disordered $K_{0.7}Mn_{0.7}Ni_{0.3}O_2$ cathode exhibits exceptional potassium storage properties, establishing the first experimental paradigm for manipulating K^+/vacancy order-disorder transition in layered cathode materials through thermodynamic-guided compositional design.

Despite exploratory efforts to understand K^+/vacancy order-disorder configurations in layered oxide cathodes, fundamental mechanistic insights remain limited. Herein, a charge-ion coupling engineering strategy is pioneered, in which modulation of the transition-metal electronic structure governs the interlayer K^+/vacancy configuration. Distinct from stoichiometry-driven tuning that relies on varying K content, charge-ion coupling regulation at a fixed K stoichiometry offers a complementary design lever for stabilizing K^+/vacancy disordering. Within the charge-ion coupling, suppressed charge ordering in the TMO_2 slabs, while avoiding appreciable TM cation ordering, is conducive to stabilizing a K^+/vacancy disordered structure. Such conditions can be realized via ionic-radius compatible substitutions, together with a substantial redox potential (Fermi level) contrast, thereby homogenizing the interlayer K-site energy landscape. To elucidate the correlation between order-to-disorder structural transformation and electrochemical charge storage performance in PIBs, a Mn/Co-based layered oxide ($K_{0.5}Mn_{0.9}Co_{0.1}O_2$) as a model system was employed. This Co-lean composition provides a kinetically robust and structurally stable layered framework, and this design concept can be extended to lower-Co or Co-free layered oxides in future studies. Leveraging the same valence nature and comparable ionic radii of Ti^{4+} (0.605 Å) and Mn^{4+} (0.530 Å) paired with their divergent redox potential ($\Delta E > 1.0$ V), we implemented Ti^{4+} substitution at Mn^{4+} sites. This substitution effect mitigates charge ordering in TMO_2 slabs through localized electron correlation modulation, thereby inducing K^+/vacancy disordering in potassium layers. Ti substitution has been widely investigated in layered Na oxides to modulate transition-metal charge ordering and the coupled Na^+/vacancy ordering [27, 29, 30]. However, it is still a mystery in K-based systems because the larger K^+ (ionic radius: 1.38 Å vs Na^+: 1.02 Å) imposes more stringent geometric and electrostatic constraints in layered K_xTMO_2. Consequently, K^+/vacancy ordering may couple more strongly with structural evolution and electrochemical degradation and shift the energetic balance between ordering-stabilized intermediates and solid-solution pathways [31]. Therefore, our work is framed as a K-based implementation and validation of this charge-ion coupling concept, rather than inferred solely from Na-layered analogues. A comparative material system comprising pristine Ti-free $K_{0.5}Mn_{0.9}Co_{0.1}O_2$ and Ti-substituted $K_{0.5}Mn_{0.8}Co_{0.1}Ti_{0.1}O_2$ to systematically investigate the structure-property relationships between K^+/vacancy ordering-disordering on their electrochemical properties, structural evolution, and K^+ kinetics toward K^+ (de)intercalation is comprehensively analyzed. The K^+/vacancy disordered $K_{0.5}Mn_{0.8}Co_{0.1}Ti_{0.1}O_2$ cathode exhibits exceptional rate performance and cycling stability, as confirmed by diverse experimental measurements, including in situ X-ray diffraction (XRD)

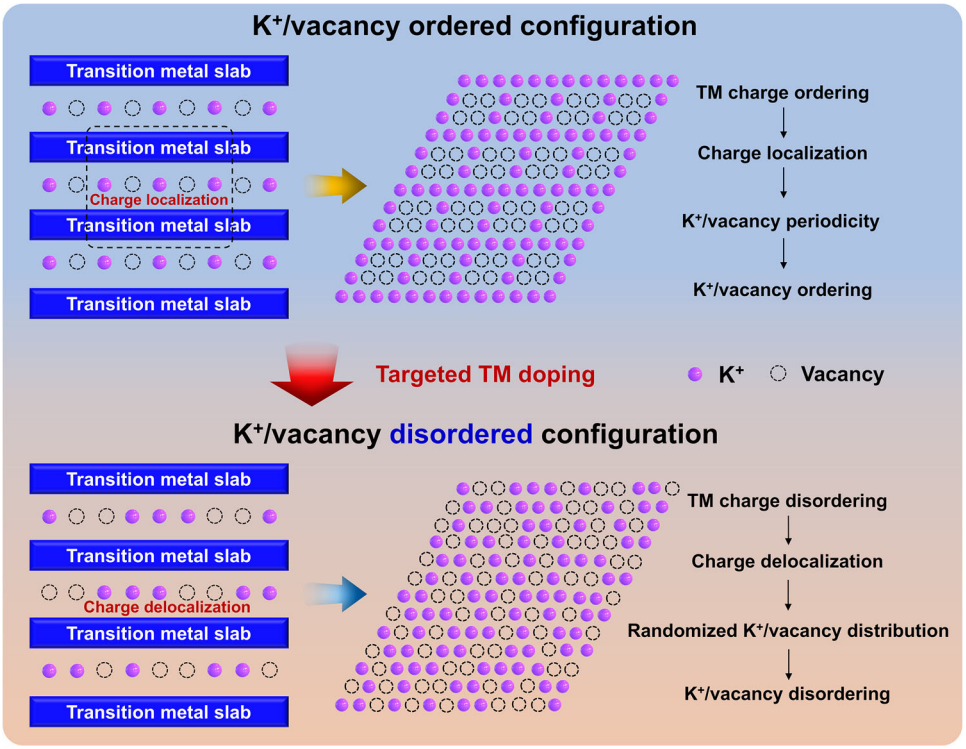

FIGURE 1 | Structure illustrations of K^+/vacancy order-disorder configurations in K_xTMO_2 and its engineering transformation routes.

characterization and dynamic analysis, exploring the intrinsic relationship between K^+/vacancy disordered interlayer structure and K^+ de-intercalation/intercalation mechanism.

2 | Results and Discussion

A series of characterizations were performed to elucidate the structure of $K_{0.5}Mn_{0.9}Co_{0.1}O_2$ and Ti-substituted $K_{0.5}Mn_{0.8}Co_{0.1}Ti_{0.1}O_2$, as displayed in Figure 2. Rietveld-refined synchrotron XRD patterns confirm that both materials adopt P3-type layered frameworks with hexagonal symmetry, as illustrated in Figure 2a,b [32]. Notably, the $K_{0.5}Mn_{0.8}Co_{0.1}Ti_{0.1}O_2$ material exhibits no detectable impurity peaks, confirming that Ti incorporation preserves the pristine crystal structure without inducing an impurity phase, thereby validating the successful metal doping. The crystallographic models show a P3-type framework with an O sublattice following an ABBCCA stacking sequence, where K^+ ions occupy prismatic sites while TM (Mn/Co/Ti) reside in octahedral coordination (Figure 2a,b; Figure S1) [17, 33]. Refined crystallographic result (Tables S1 and S2) indicates uniform occupancy of Mn, Co, and Ti in TM octahedral sites, with unit-cell parameters shifting from $a = b = 2.8939$ Å, $c = 21.2010$ Å (pristine) to $a = b = 2.8814$ Å, $c = 20.9929$ Å (Ti-substituted), consistent with lattice modulation upon substitution. The refined lattice parameters and the corresponding c-axis decomposition into the interlayer K-layer spacing and TMO_2 slab thickness are presented in Figure S2, providing structural information relevant to K^+ transport. Inductively coupled plasma (ICP) analysis reveals stoichiometric ratios of K: Mn: Co = 5.03: 9.02: 1.00 in $K_{0.5}Mn_{0.9}Co_{0.1}O_2$ and K: Mn: Co: Ti = 4.95: 8.07: 1.00: 1.06 in $K_{0.5}Mn_{0.8}Co_{0.1}Ti_{0.1}O_2$, closely matching the nominal compositions with precision in Ti doping levels (Table S3). The delocalized electron via Ti doping is verified by partial electron localization function (PELF) maps (Figure 2c), where it provides a real-space measure of electron localization within the TM-O framework. Compared to $K_{0.5}Mn_{0.9}Co_{0.1}O_2$, the Ti-substituted $K_{0.5}Mn_{0.8}Co_{0.1}Ti_{0.1}O_2$ exhibits a less spatially confined PELF distribution across the TM slab plane, indicating enhanced electron delocalization in the TM-O network. Meanwhile, the dashed region highlights the Ti dopant site in Figure 2d, the deformation charge density (charge-density difference) visualizations (Figure 2d) directly reveal Ti-induced charge redistribution in real space. Upon Ti substitution, the accumulation/depletion pattern is distinctly re-patterned near the substituted site, evidencing an altered local polarization/charge landscape within the TM-O framework. Density Functional Theory (DFT)-based Projected Density of States (PDOS) analyses further show a broadening of Mn 3d states, consistent with enhanced delocalization and reduced electronic localization (Figure S3). Moreover, to elucidate the Ti-induced evolution of transition-metal valence and local coordination environments, we performed synchrotron Mn/Co K-edge X-ray Absorption Near Edge Structure (XANES) and Extended X-ray Absorption Fine Structure (EXAFS) measurements (Figure 2e,f; Figure S4). Mn K-edge spectra indicate that Mn shows a mixed Mn^{3+}/Mn^{4+} state with a subtle edge shift to lower energy upon Ti substitution, whereas the Co K-edge spectra are essentially superimposable and closely resemble Co_2O_3, consistent with predominantly Co^{3+}. Mn/Co K-edge EXAFS confirms preserved octahedral TM-O coordination in both materials, while the increase σ^2 observed upon Ti substitution indicates enhanced local disorder, manifested as damping of higher-shell contributions and reduced structural coherence beyond the first coordination shell. Within the charge-ion coupling framework, this local disorder is consistent with

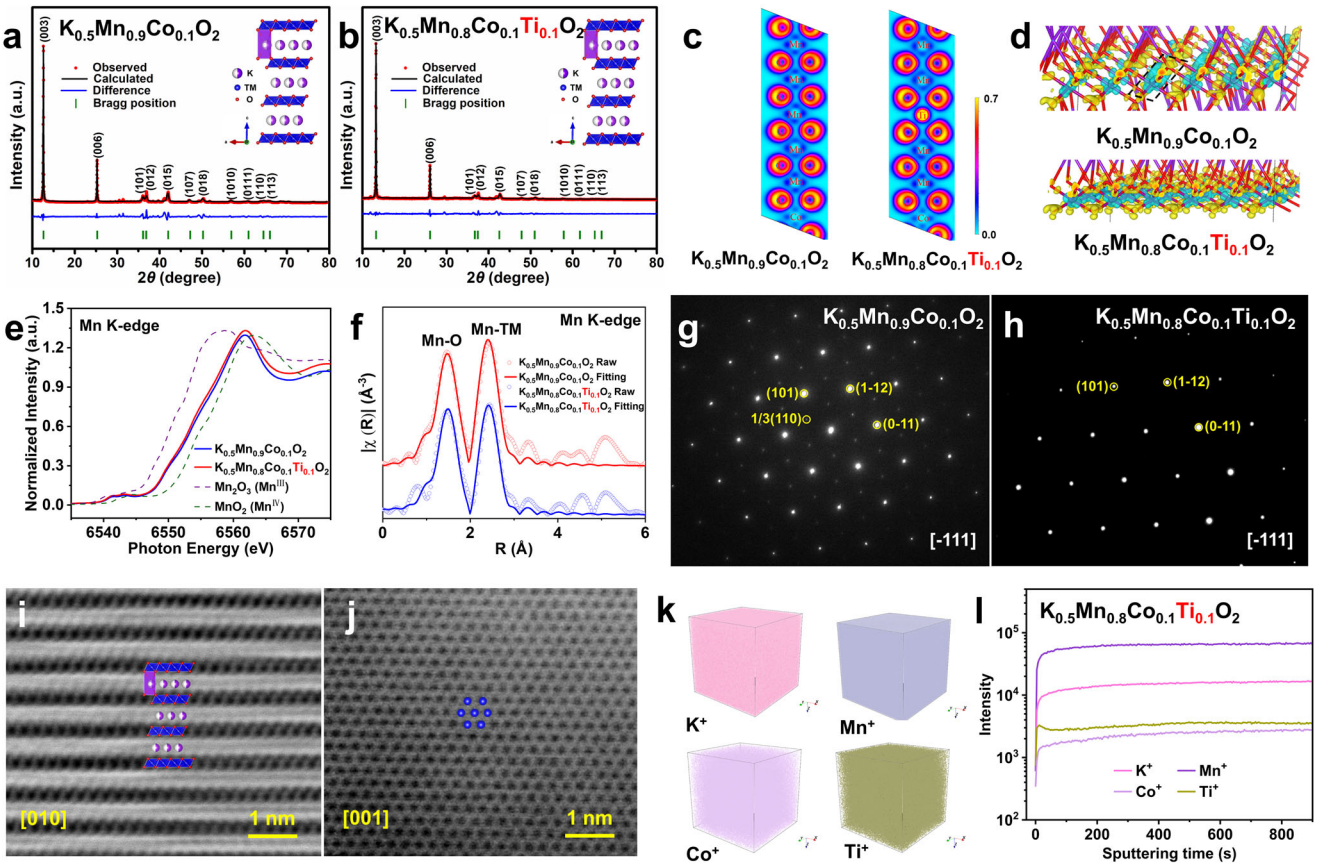

FIGURE 2 | Structural characterizations of $K_{0.5}Mn_{0.9}Co_{0.1}O_2$ and $K_{0.5}Mn_{0.8}Co_{0.1}Ti_{0.1}O_2$. XRD Rietveld refinement of (a) $K_{0.5}Mn_{0.9}Co_{0.1}O_2$ and (b) $K_{0.5}Mn_{0.8}Co_{0.1}Ti_{0.1}O_2$ (inset: crystal structure viewed). (c) Two-dimensional maps of the partial electron localization function on the TM slab plane for $K_{0.5}Mn_{0.9}Co_{0.1}O_2$ and $K_{0.5}Mn_{0.8}Co_{0.1}Ti_{0.1}O_2$. (d) Deformation charge density (charge-density difference) visualizations for $K_{0.5}Mn_{0.9}Co_{0.1}O_2$ and $K_{0.5}Mn_{0.8}Co_{0.1}Ti_{0.1}O_2$, where yellow and cyan indicate electron accumulation and depletion, respectively. (e) Normalized XANES spectra and (f) corresponding EXAFS spectra at the Mn K-edges of $K_{0.5}Mn_{0.9}Co_{0.1}O_2$ and $K_{0.5}Mn_{0.8}Co_{0.1}Ti_{0.1}O_2$. SAED patterns of (g) $K_{0.5}Mn_{0.9}Co_{0.1}O_2$ and (h) $K_{0.5}Mn_{0.8}Co_{0.1}Ti_{0.1}O_2$ along the [$\bar{1}$11] zone axis. ABF-STEM image of $K_{0.5}Mn_{0.8}Co_{0.1}Ti_{0.1}O_2$ along the (i) [010] and (j) [001] zone axis. (k) TOF-SIMS 3D images of the sputtered volume corresponding to the depth profiles in the $K_{0.5}Mn_{0.8}Co_{0.1}Ti_{0.1}O_2$: K^+ Mn^+, Co^+, and Ti^+. (l) Depth profile of K^+ Mn^+, Co^+ and Ti^+ obtained by sputtering.

reduced charge-ordering tendencies and a more homogenized interlayer K-site energy landscape that disfavors commensurate K^+/vacancy superstructures. Importantly, the [$\bar{1}$11] zone-axis selected-area electron diffraction (SAED) patterns reveal superlattice spots (e.g. 1/3(110)) in $K_{0.5}Mn_{0.9}Co_{0.1}O_2$ arising from the K^+/vacancy ordered structure, whereas the absence of such spots in $K_{0.5}Mn_{0.8}Co_{0.1}Ti_{0.1}O_2$ confirms a disordered structure (Figure 2g,h).

Aberration-corrected scanning transmission electron microscopy (STEM) with annular bright-field (ABF) and high-angle annular dark-field (HAADF) detectors provides detailed atomic-scale crystal structure information about $K_{0.5}Mn_{0.8}Co_{0.1}Ti_{0.1}O_2$. ABF-STEM images along [010] show alternating K and TM layers with ABBCCA stacking (Figure 2i), aligning with the atomic model of the P3-type structure. The HAADF-STEM images show an interlayer spacing of ~0.70 nm, matching the interslab distance from XRD refinement data (Figure S5a). Along the [001] zone axis, the ABF-STEM image shows that the TM atoms form hexagonal symmetry in their arrangement (Figure 2j). In HAADF-STEM observations, the spacing between adjacent TM atoms is measured to be 0.29 nm, corresponding to the lattice parameter *a* (2.8814 Å) (Figure S5b). Scanning electron microscopy (SEM) and transmission electron microscopy (TEM) images (Figure S6) reveal that both $K_{0.5}Mn_{0.9}Co_{0.1}O_2$ and $K_{0.5}Mn_{0.8}Co_{0.1}Ti_{0.1}O_2$ materials show particles with an average diameter of ~1 μm. High-resolution TEM (HRTEM) images show interlayer distances measured at 0.242 and 0.240 nm, respectively, which align well with the (012) plane of the P3-type layered structure (Figure S7). Notably, the three-dimensional elemental distribution of $K_{0.5}Mn_{0.8}Co_{0.1}Ti_{0.1}O_2$ was examined by using time-of-flight secondary ion mass spectrometry (TOF-SIMS), which provided both depth and spatial profiles of the constituent (Figure 2k). The K^+, Mn^+, Co^+, and Ti^+ signals show nearly constant intensities over a 900 s sputtering period (Figure 2l), indicating a uniform elemental distribution across the near-surface region. Comparable TOF-SIMS results for $K_{0.5}Mn_{0.9}Co_{0.1}O_2$ are shown in Figures S8 and S9. Moreover, the energy dispersive spectroscopy (EDS) mapping images confirm homogeneous distribution of K, Mn, Co, Ti, and O throughout the particles (Figure S10).

Electrochemical performance was evaluated for both materials as PIB cathodes over 1.5–3.9 V (vs K^+/K) (Figure 3). The $K_{0.5}Mn_{0.9}Co_{0.1}O_2$ shows four pairs of redox peaks at 2.27/1.99,

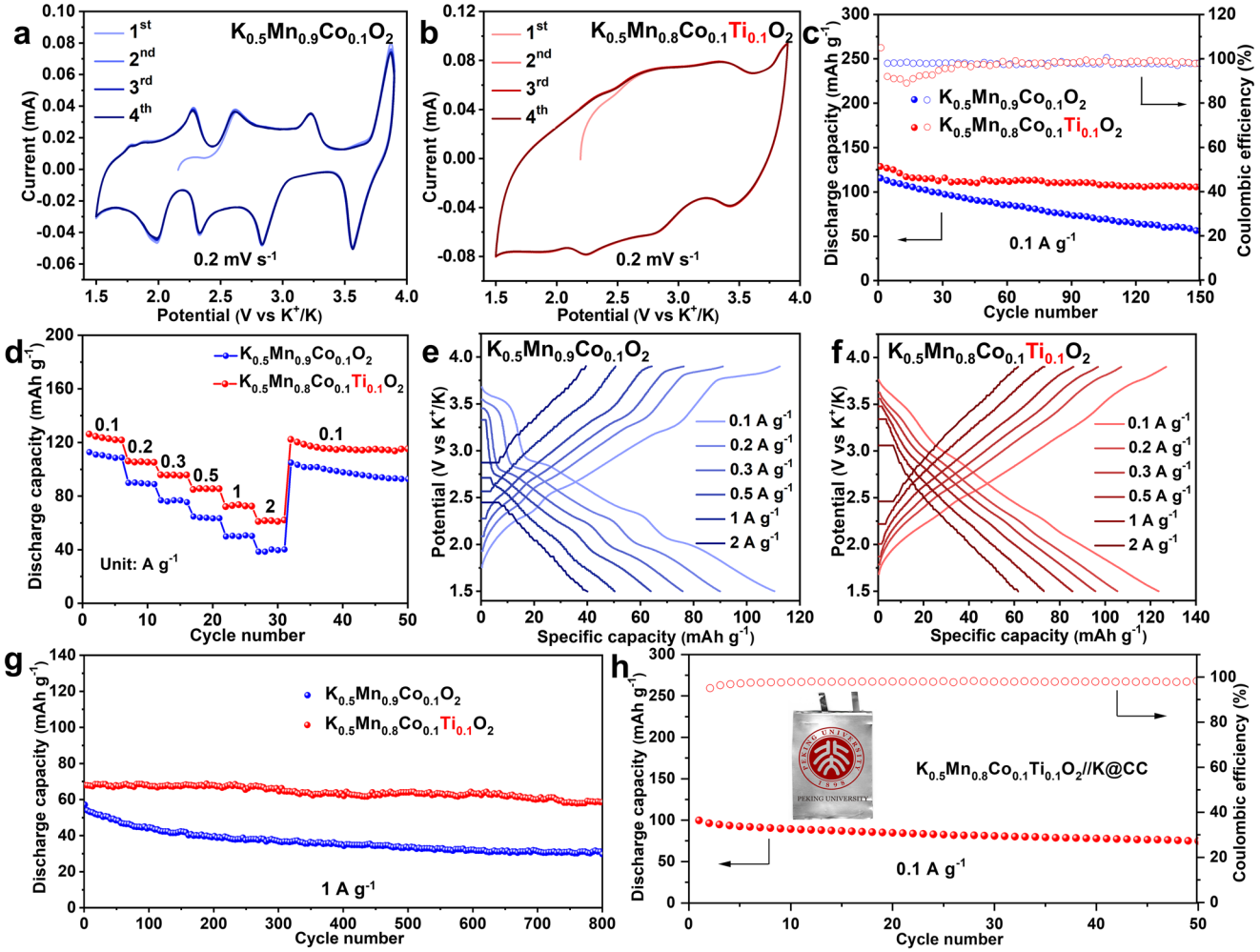

FIGURE 3 | Electrochemical performances of $K_{0.5}Mn_{0.9}Co_{0.1}O_2$ and $K_{0.5}Mn_{0.8}Co_{0.1}Ti_{0.1}O_2$ in 1.5–3.9 V (vs K^+/K). CV curves of the first four cycles at 0.2 mV s^{-1} of (a) $K_{0.5}Mn_{0.9}Co_{0.1}O_2$ and (b) $K_{0.5}Mn_{0.8}Co_{0.1}Ti_{0.1}O_2$. (c) Cycling performance with the Coulombic efficiencies measured at 0.1 A g^{-1}. (d) Rate performance conducted at 0.1, 0.2, 0.3, 0.5, 1, 2, and back to 0.1 A g^{-1}. The corresponding charge/discharge curves of (e) $K_{0.5}Mn_{0.9}Co_{0.1}O_2$ and (f) $K_{0.5}Mn_{0.8}Co_{0.1}Ti_{0.1}O_2$ at different rates. (g) Long-term cyclic performance of $K_{0.5}Mn_{0.9}Co_{0.1}O_2$ and $K_{0.5}Mn_{0.8}Co_{0.1}Ti_{0.1}O_2$ at 1 A g^{-1}. (h) Cycling performance of the K-ion pouch cell based on $K_{0.5}Mn_{0.8}Co_{0.1}Ti_{0.1}O_2$ cathode and K@CC anode at 0.1 A g^{-1} (inset: digital photos of K-ion pouch cell).

2.62/2.33, 3.23/2.83, and 3.87/3.56 V in CV curves, attributed to K^+/vacancy ordering between adjacent TMO_2 slabs (Figure 3a) [28, 34]. By contrast, Ti-substituted $K_{0.5}Mn_{0.8}Co_{0.1}Ti_{0.1}O_2$ resembles that of capacitors with a single broad redox peak, indicating suppression of K^+/vacancy ordering upon Mn/Co/Ti mixing (Figure 3b) [27]. Similarly, galvanostatic charge-discharge profiles of $K_{0.5}Mn_{0.9}Co_{0.1}O_2$ reveal four voltage plateaus arising from multiple K^+/vacancy ordering in K layers (Figure S11a). By comparison, those of $K_{0.5}Mn_{0.8}Co_{0.1}Ti_{0.1}O_2$ transform into fully sloping curves, and four voltage plateaus totally disappeared, which results from a solid-solution reaction without a K^+/vacancy ordered superstructure, as discussed later (Figure S11b).

The K^+/vacancy disordered $K_{0.5}Mn_{0.8}Co_{0.1}Ti_{0.1}O_2$ delivers a higher initial discharge specific capacity of 128.8 mAh g^{-1} and excellent cycling performance, retaining 82.5% after 150 cycles at 0.1 A g^{-1} (Figure 3c). In contrast, the $K_{0.5}Mn_{0.9}Co_{0.1}O_2$ with ordered superstructure shows a lower initial capacity of 116.2 mAh g^{-1} and suffers from severe fading to 56.6 mAh g^{-1} over 150 cycles, resulting in a capacity retention of only 48.7%. Notably, the higher capacity of the K^+/vacancy disordered $K_{0.5}Mn_{0.8}Co_{0.1}Ti_{0.1}O_2$ can be rationalized by an expanded thermodynamically accessible range of reversible K (de)intercalation. This originates from the suppression of K^+/vacancy ordering, which mitigates ordering-induced K^+ storage obstacles by reducing the site-energy disparity among K sites and enabling more reversibly accessible K-storage sites/states [28]. Further evaluation of rate capability exhibits that the $K_{0.5}Mn_{0.8}Co_{0.1}Ti_{0.1}O_2$ delivers discharge capacities of 123.6, 105.4, 95.8, 85.5, and 72.7 mAh g^{-1} at 0.1, 0.2, 0.3, 0.5, and 1 A g^{-1}, respectively, with a retained capacity of 61.7 mAh g^{-1} even at 2 A g^{-1} (Figure 3d). Upon returning to 0.1 A g^{-1}, the capacity recovers to 120.3 mAh g^{-1}, indicating excellent high-rate stability and reversibility. Across all tested current densities, $K_{0.5}Mn_{0.8}Co_{0.1}Ti_{0.1}O_2$ consistently delivers higher discharge capacities than $K_{0.5}Mn_{0.9}Co_{0.1}O_2$, with the advantage becoming more pronounced at higher current densities. Moreover, $K_{0.5}Mn_{0.9}Co_{0.1}O_2$ exhibits evident voltage polarization with increasing current density (Figure 3e). All voltage plateaus are completely suppressed at exceeding 1 A g^{-1}, leading to further capacity decay. By contrast, $K_{0.5}Mn_{0.8}Co_{0.1}Ti_{0.1}O_2$ displays negligible polarization, implying ultrafast K^+ storage

and low polarization (Figure 3f). Impressively, the K^+/vacancy disordered $K_{0.5}Mn_{0.8}Co_{0.1}Ti_{0.1}O_2$ exhibits exceptional long-term cyclic stability, retaining a capacity of 58.6 mAh g^{-1} even over 800 cycles at 1 A g^{-1} with a capacity retention of 86.2% and an average capacity loss of 0.017% per cycle (Figure 3g; Figure S12). By comparison, the $K_{0.5}Mn_{0.9}Co_{0.1}O_2$ shows rapid capacity decay from 54.1 to 29.3 mAh g^{-1} over 800 cycles, corresponding to capacity retention of 54.2%. Moreover, the $K_{0.5}Mn_{0.8}Co_{0.1}Ti_{0.1}O_2$ was further evaluated at 0.2 and 0.5 A g^{-1}, delivering 84.4% capacity retention over 200 cycles and 83.0% over 400 cycles, respectively (Figure S13). Post-cycling SEM images of $K_{0.5}Mn_{0.9}Co_{0.1}O_2$ and $K_{0.5}Mn_{0.8}Co_{0.1}Ti_{0.1}O_2$ are provided in Figure S14. These results demonstrate that K^+/vacancy disordering not only accelerates K^+ storage but also dramatically enhances long-term cycling stability. Compared with previously reported layered oxide cathodes, the K^+/vacancy disordered $K_{0.5}Mn_{0.8}Co_{0.1}Ti_{0.1}O_2$ exhibits highly competitive electrochemical performance in PIBs (Table S4).

To show the practical aspects, the K-ion pouch cells were assembled by using $K_{0.5}Mn_{0.8}Co_{0.1}Ti_{0.1}O_2$ as the cathode and carbon-cloth-based potassium composite (K@CC) as the anode (Figure S15a). A fully charged pouch cell continuously powered the light-emitting diodes (LEDs) over an extended period (Figure S15b). The charge-discharge voltage profiles of the pouch cell resemble those of $K_{0.5}Mn_{0.8}Co_{0.1}Ti_{0.1}O_2$, featuring smoothly sloping curves without distinct voltage plateaus (Figure S15c). Based on the mass of cathode material, the pouch cell shows an initial discharge specific capacity of 82.4 mAh g^{-1}, with a reversible discharge capacity of 74.9 mAh g^{-1} after 50 cycles (87% of the initial capacity) (Figure 3h). This demonstrates stable cyclability and minimal voltage decay of the pouch cell, highlighting the advantages of K^+/vacancy disordering for $K_{0.5}Mn_{0.8}Co_{0.1}Ti_{0.1}O_2$.

The structure evolution of $K_{0.5}Mn_{0.9}Co_{0.1}O_2$ and $K_{0.5}Mn_{0.8}Co_{0.1}Ti_{0.1}O_2$ during K^+ de-intercalation/intercalation was monitored by in situ XRD measurement. Upon changing from open-circuit voltage (or 1.5 V) to 3.9 V, the (006) peak of $K_{0.5}Mn_{0.8}Co_{0.1}Ti_{0.1}O_2$ shifts progressively toward low angle, while the (101), (012), and (015) peaks shift to high angle (Figure 4a–c). These phenomena originate from *c*-axis expansion and *a*-*b* plane contraction, driven by enhanced electrostatic repulsion between O layers upon K^+ extraction [35]. Upon K^+ insertion to 1.5 V, the (006) peak re-shifts to high angle region, while the (101), (012), and (015) peaks shift toward low angle region, demonstrating the reduced electrostatic repulsion between oxygen upon K^+ insertion. Notably, the (101), (012), and (015) diffraction peaks of $K_{0.5}Mn_{0.8}Co_{0.1}Ti_{0.1}O_2$ exhibited a modest decrease in intensity throughout both high and low voltage states, yet all peaks remained discernible without complete extinction or the emergence of new diffraction peaks. This indicates that K^+/vacancy-disordered $K_{0.5}Mn_{0.8}Co_{0.1}Ti_{0.1}O_2$ undergoes a reversible single-phase solid-solution reaction during K^+ de-intercalation/intercalation, demonstrating robust structural stability.

The structure evolution of $K_{0.5}Mn_{0.9}Co_{0.1}O_2$ is similar to that of $K_{0.5}Mn_{0.8}Co_{0.1}Ti_{0.1}O_2$, with three key distinctions (Figure 4d–f). First, the (101), (012), and (015) peaks weaken without vanishing, and a new peak at 40.4° appears upon charging to 3.3 V and discharging to 2.8 V. This new peak is assigned to the (104) plane of the O3 phase, indicating a P3-to-O3 phase transformation for $K_{0.5}Mn_{0.9}Co_{0.1}O_2$ at high potential [36]. Second, the (101), (012), and (015) peaks of $K_{0.5}Mn_{0.9}Co_{0.1}O_2$ exhibit more complex shift behavior within the blue dashed region (discharging from 2.4 to 1.5 V followed by charging to 2.9 V). The (101) peak undergoes a low-angle shift, then a high-angle shift upon discharging, before stabilizing and reverses upon charging. The (012) peak exhibits opposite behavior—first shifting to high angle, then to low angle, and stabilizing during discharging, with reverse shifts during charging—forming a mirror-symmetric relationship with the (101) peak variations. The (015) peak displays even greater complexity: it first disappears at the initial discharging stage, then two new diffraction peaks emerge near 41.5° and 41.9°; these new peaks subsequently vanish, and the P3-phase (015) peak reappears, only to disappear again at the end of the charging stage in this region, with the two new peaks re-emerging. Based on current understanding, the disappearance of the (015) peak and emergence of the two new peaks indicate the formation of an uncharacterized phase, denoted here as "X." Therefore, the $K_{0.5}Mn_{0.9}Co_{0.1}O_2$ undergoes a complex phase transition: P3→X→P3→X→P3 within the blue dashed region, with phase "X" requiring further investigation. Third, the *a* and *c* lattice parameters of $K_{0.5}Mn_{0.9}Co_{0.1}O_2$ show significant fluctuations at positions corresponding to charge-discharge voltage plateaus, in contrast to the smooth and fluctuation-free variations in the lattice parameters of $K_{0.5}Mn_{0.8}Co_{0.1}Ti_{0.1}O_2$ (Figure S16). Therefore, the K^+/vacancy ordered $K_{0.5}Mn_{0.9}Co_{0.1}O_2$ exhibits complex phase transitions during charge-discharge cycles, indicating the rearrangement of the K^+/vacancy ordered structure during K^+ de-intercalation/intercalation.

X-ray photoelectron spectroscopy (XPS) was performed to elucidate the electrochemical mechanism during K^+ deintercalation/intercalation. For $K_{0.5}Mn_{0.9}Co_{0.1}O_2$, the Mn $2p_{3/2}$ spectra consist of Mn^{3+} (642.0 eV) and Mn^{4+} (642.64 eV), and the Mn $2p_{1/2}$ spectrum shows the peaks at 653.3 and 654.3 eV, indicating the coexistence of Mn^{3+} and Mn^{4+} (Figure S17a) [37–39]. The Mn spectrum in $K_{0.5}Mn_{0.8}Co_{0.1}Ti_{0.1}O_2$ also exhibits mixed +3 and +4 valences, with a higher Mn^{3+} content than that in $K_{0.5}Mn_{0.9}Co_{0.1}O_2$, suggesting that Ti doping lowers the valence state of Mn. In the Co 2p spectra of both materials, the peaks at 780.28 and 795.21 eV are assigned to Co $2p_{3/2}$ and Co $2p_{1/2}$, respectively, demonstrating that the Co oxidation state is +3 [40], while the valence state of Co is retained after Ti doping (Figure S17b). The Ti 2p spectrum of $K_{0.5}Mn_{0.8}Co_{0.1}Ti_{0.1}O_2$ shows a Ti^{4+} binding energies, which two peaks at 457.8 and 463.6 eV are assigned to Ti $2p_{3/2}$ and Ti $2p_{1/2}$, respectively [41] (Figure S17c). During the charging process, the Mn spectrum of $K_{0.5}Mn_{0.8}Co_{0.1}Ti_{0.1}O_2$ shows apparent shifts toward the higher binding energy region, indicating the oxidation of Mn (Figure 4g). Followed by discharging to 1.5 V, the peaks shift toward the lower binding energy region, suggesting the reduction of Mn. The same trend is observed in the Co spectra, with peaks shifting to higher binding energies during charging—indicating oxidation—and to lower binding energies during discharge—indicating reduction (Figure 4h). Notably, the Ti 2p spectrum of $K_{0.5}Mn_{0.8}Co_{0.1}Ti_{0.1}O_2$ shows no apparent changes, indicating that the Ti^{4+} is electrochemically inactive (Figure 4i). Similar Mn and Co peak shift behaviors are observed for $K_{0.5}Mn_{0.9}Co_{0.1}O_2$, as shown in Figure S18. Therefore, the electrochemically active Mn and Co species provide charge compensation upon K^+ (de)intercalation, and the doped Ti remains tetravalent in the Mn-Co-based layered oxides.

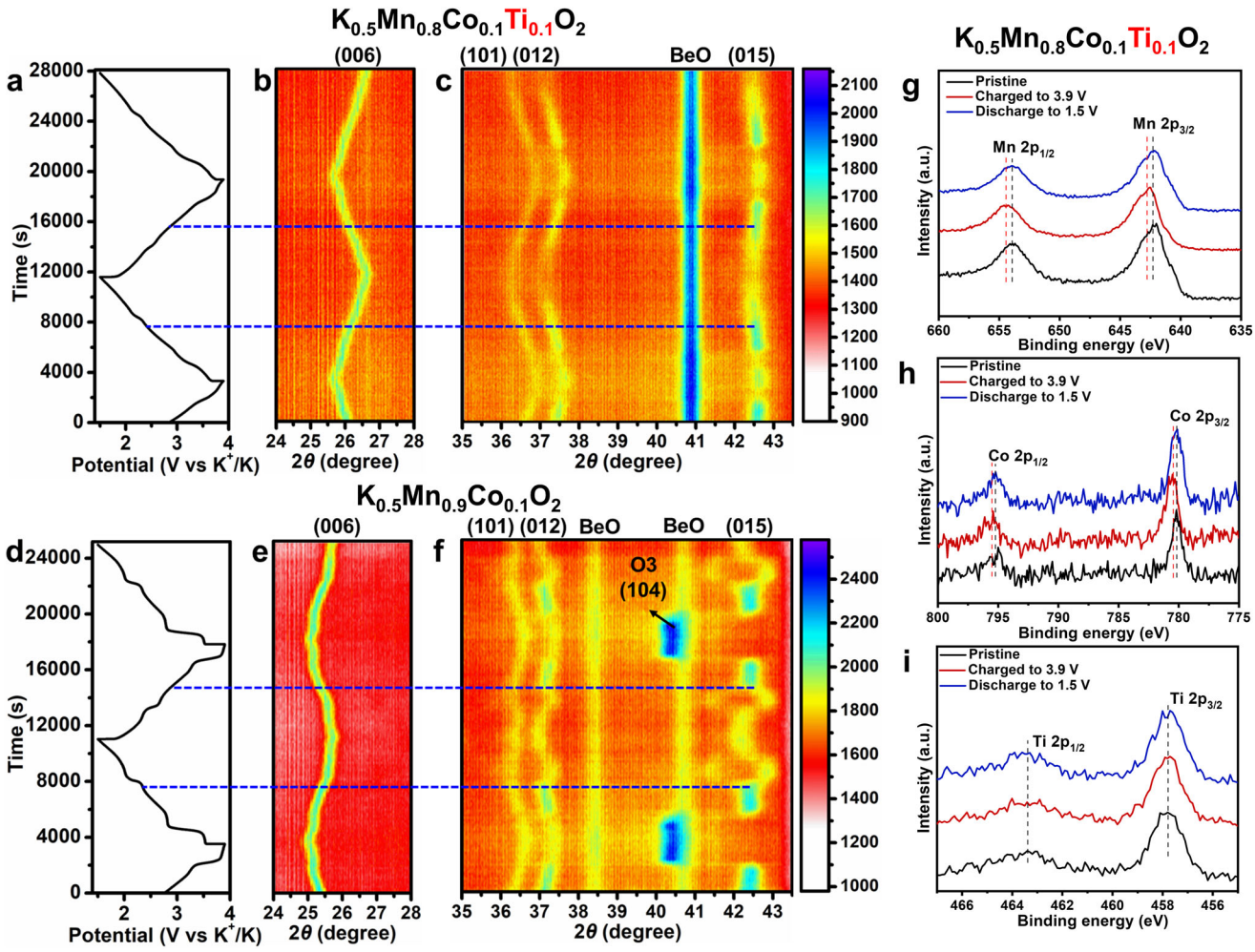

FIGURE 4 | In situ XRD and ex situ XPS characterizations of $K_{0.5}Mn_{0.9}Co_{0.1}O_2$ and $K_{0.5}Mn_{0.8}Co_{0.1}Ti_{0.1}O_2$. Charge/discharge curves during the first two cycles at 0.05 A g^{-1} in 1.5–3.9 V of (a) $K_{0.5}Mn_{0.8}Co_{0.1}Ti_{0.1}O_2$ and (d) $K_{0.5}Mn_{0.9}Co_{0.1}O_2$. (b, c) Two-dimensional in situ XRD patterns at 24–28° and 35–43.5° of $K_{0.5}Mn_{0.8}Co_{0.1}Ti_{0.1}O_2$. (e, f) Two-dimensional in situ XRD patterns at 24–28° and 35–43.5° of $K_{0.5}Mn_{0.9}Co_{0.1}O_2$. XPS spectra of (g) Mn 2p, (h) Co 2p, and (i) Ti 2p for $K_{0.5}Mn_{0.8}Co_{0.1}Ti_{0.1}O_2$ at different charge/discharge states.

Moreover, cycling-state (ex situ) SAED acquired along the [$\bar{1}$11] zone axis shows that the K^+/vacancy-ordering fingerprints are preserved during cycling: superlattice reflections (e.g., 1/3(110)) persist for $K_{0.5}Mn_{0.9}Co_{0.1}O_2$ after charging to 3.9 V and subsequent discharging to 1.5 V, whereas no superlattice spots emerge for $K_{0.5}Mn_{0.8}Co_{0.1}Ti_{0.1}O_2$ (Figure S19). These observations indicate retention of the respective ordered-disordered interlayer configurations, with no detectable order-disorder interconversion under the tested conditions.

To investigate the effect of K^+/vacancy disorder on ion-diffusion kinetics, the galvanostatic intermittent titration technique (GITT) was employed (Figure S20). The theoretical initial discharge specific capacities of $K_{0.5}Mn_{0.9}Co_{0.1}O_2$ and $K_{0.5}Mn_{0.8}Co_{0.1}Ti_{0.1}O_2$ are 125.8 mAh g^{-1} (0.50 mol K^+ per unit formula) and 144.9 mAh g^{-1} (0.57 mol K), respectively (Figure S20a,b). The K^+ diffusion coefficients of $K_{0.5}Mn_{0.8}Co_{0.1}Ti_{0.1}O_2$ are calculated to range from 10^{-12} to 10^{-11} cm^2 s^{-1}, one order of magnitude higher than those of $K_{0.5}Mn_{0.9}Co_{0.1}O_2$ (10^{-13} to 10^{-12} cm^2 s^{-1}) (Figure S20c). Notably, the K^+ diffusion coefficient of $K_{0.5}Mn_{0.8}Co_{0.1}Ti_{0.1}O_2$ exhibits no abrupt changes, consistent with the smooth characteristic of its charge/discharge profiles, a feature afforded by K^+/vacancy disordering. The fitting results show that the charge-transfer resistance of $K_{0.5}Mn_{0.8}Co_{0.1}Ti_{0.1}O_2$ (504.9 Ω) is markedly lower than that of $K_{0.5}Mn_{0.9}Co_{0.1}O_2$ (849.7 Ω), indicating faster interfacial charge-transfer and K^+ transport kinetics in the K^+/vacancy-disordered cathode (Figure S21 and Table S5).

Molecular dynamic simulation calculations were conducted to examine the K^+ diffusion pathways in the K^+/vacancy disordered $K_{0.5}Mn_{0.8}Co_{0.1}Ti_{0.1}O_2$, and K^+/vacancy ordered $K_{0.5}Mn_{0.9}Co_{0.1}O_2$, revealing distinct ionic migration properties as visualized in Figure 5a,b. The corresponding top-view analysis of K^+ migration trajectories within individual K layer reveals that the $K_{0.5}Mn_{0.8}Co_{0.1}Ti_{0.1}O_2$ exhibits a percolative diffusion network with enhanced spatial continuity compared to $K_{0.5}Mn_{0.9}Co_{0.1}O_2$. These simulations demonstrate that the K^+/vacancy disordering establishes interconnected ion-transport channels, thereby facilitating accelerated ionic diffusion kinetics in the disordered $K_{0.5}Mn_{0.8}Co_{0.1}Ti_{0.1}O_2$.

Based on structural characterization, electrochemical measurements, electrochemical mechanism analysis, and K^+ transport kinetics investigations, the K^+/vacancy configurations of

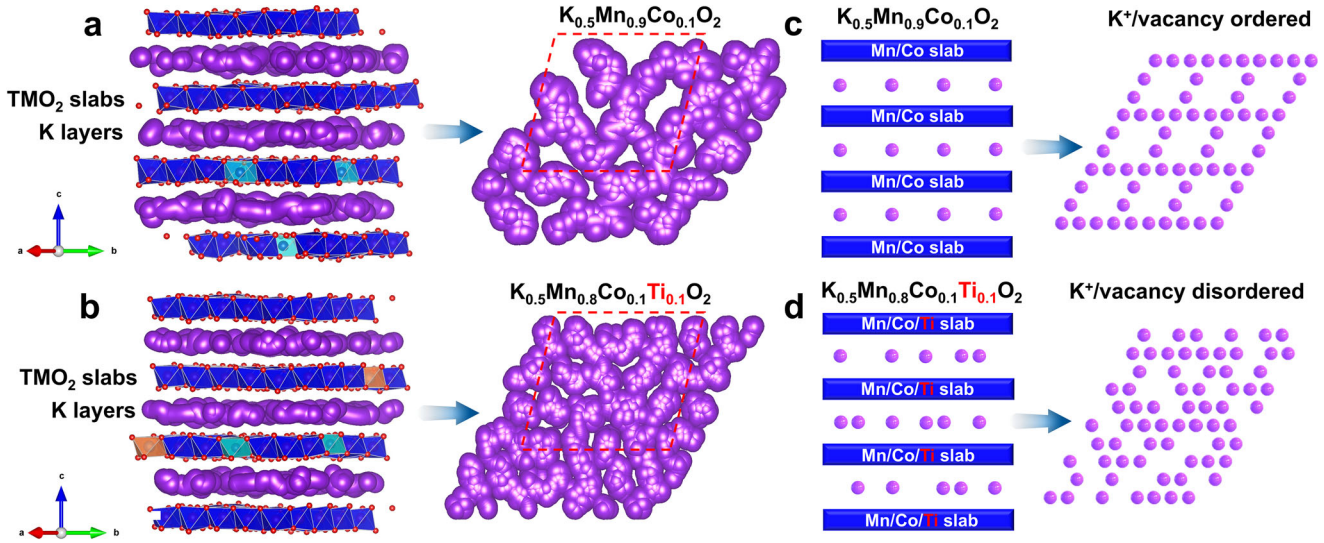

FIGURE 5 | Molecular dynamic simulation calculations and K^+/vacancy structure illustration of $K_{0.5}Mn_{0.9}Co_{0.1}O_2$ and $K_{0.5}Mn_{0.8}Co_{0.1}Ti_{0.1}O_2$. Trajectories simulation of K^+ in (a) $K_{0.5}Mn_{0.9}Co_{0.1}O_2$ and (b) $K_{0.5}Mn_{0.8}Co_{0.1}Ti_{0.1}O_2$, the right panel figure is the top view of each K layer. K^+/vacancy structure illustrations of (c) $K_{0.5}Mn_{0.9}Co_{0.1}O_2$ and (d) $K_{0.5}Mn_{0.8}Co_{0.1}Ti_{0.1}O_2$. The purple balls represent K^+.

$K_{0.5}Mn_{0.9}Co_{0.1}O_2$ and $K_{0.5}Mn_{0.8}Co_{0.1}Ti_{0.1}O_2$ are schematically depicted in Figure 5c,d, respectively. The distribution of K^+ and vacancies of $K_{0.5}Mn_{0.9}Co_{0.1}O_2$ displays distinct periodicity with their positions fixed, forming a K^+/vacancy ordered structure (Figure 5c). In sharp contrast, the positions and arrangement of K^+ and vacancies in $K_{0.5}Mn_{0.8}Co_{0.1}Ti_{0.1}O_2$ exhibit randomness, indicating the K^+/vacancy disordered structure (Figure 5d).

3 | Conclusion

In summary, a charge-ion coupling engineering strategy has been utilized to construct a fully K^+/vacancy disordered $K_{0.5}Mn_{0.8}Co_{0.1}Ti_{0.1}O_2$ cathode for PIBs through metal doping. The Ti^{4+} substitution for Mn^{4+} in Mn/Co-based layered oxide—leveraging identical valence state and disparate redox potential—effectively suppresses inherent charge ordering, thereby inducing K^+/vacancy disordering. As a result, the K^+/vacancy disordered P3-type $K_{0.5}Mn_{0.8}Co_{0.1}Ti_{0.1}O_2$ exhibits exceptional rate capability (61.7 mAh g^{-1} at 2 A g^{-1}) and outstanding long-term cycling stability over 800 cycles at 1 A g^{-1} compared to ordered $K_{0.5}Mn_{0.9}Co_{0.1}O_2$. The as-prepared K-ion pouch cell, employed with $K_{0.5}Mn_{0.8}Co_{0.1}Ti_{0.1}O_2$ cathode, also stabilizes dozens of cycles. Mechanistically, in situ XRD measurement reveals that the K^+/vacancy disordered $K_{0.5}Mn_{0.8}Co_{0.1}Ti_{0.1}O_2$ undergoes a highly reversible single-phase reaction during K^+ deintercalation/intercalation, enhancing structural stability and thus improving long-term cycling performance. Transport kinetics analyses further demonstrate that the enhanced rate capability originates from the interconnected K^+ diffusion channels and accelerated K^+ transport kinetics enabled by the K^+/vacancy disordered structure. Our research establishes an efficient approach for designing K^+/vacancy layered oxide cathode materials, facilitating practical high-rate and long-cycling-life PIBs. More broadly, charge-ion coupling regulation provides a transferable, mechanism-guided route to control K^+/vacancy ordering-disordering, and earth-abundant, radius-compatible substitutions that introduce redox-potential contrast represent a clear direction for future development.

Acknowledgements

This research was funded by the National Key Research and Development Program of China (Grant No. 2023YFB3809300), the National Science Foundation of China (Grant No. 52373306), the Key Research and Development Program Project of Hubei Province (Grant Number. 2023BAB140), the Natural Science Foundation of Hubei Province (Grant Nos. 2023AFA053, 2024BAA013), the Key Research and Development Program of Henan Province (Grant No. 251111240100), Open Project of Inner Mongolia Engineering Research Center of Lithium-Sulfur Battery Energy Storage (No. MDK2025071) as well as Opening funding from Key Laboratory of Engineering Dielectrics and Its Application (Harbin University of Science and Technology) (No. KFM202507, Ministry of Education). Dr. Jian Wang also acknowledges the fellowship supported by the Alexander von Humboldt Foundation. We also thank Dr. Ke Yang and Dr. Haitao Liu for the discussion of simulation results.

Open access funding enabled and organized by Projekt DEAL.

Conflicts of Interest

The authors declare no conflicts of interest.

Data Availability Statement

The data that support the findings of this study are available from the corresponding author upon reasonable request.

References

1. Y. Xu, Y. Du, H. Chen, et al., "Recent Advances in Rational Design for High-Performance Potassium-Ion Batteries," *Chemical Society Reviews* 53 (2024): 7202–7298, https://doi.org/10.1039/D3CS00601H.

2. M. Li, C. Wang, C. Wang, et al., "10 Years Development of Potassium-Ion Batteries," *Advanced Materials* 37 (2025): 2416717, https://doi.org/10.1002/adma.202416717.

3. T. Hosaka, K. Kubota, A. S. Hameed, and S. Komaba, "Research Development on K-Ion Batteries," *Chemical Reviews* 120 (2020): 6358–6466, https://doi.org/10.1021/acs.chemrev.9b00463.

4. X. Min, J. Xiao, M. Fang, et al., "Potassium-Ion Batteries: Outlook on Present and Future Technologies," *Energy & Environmental Science* 14 (2021): 2186–2243, https://doi.org/10.1039/D0EE02917C.

5. J. Sun, Y. Du, Y. Liu, et al., "Recent Advances in Potassium Metal Batteries: Electrodes, Interfaces and Electrolytes," *Chemical Society Reviews* 54 (2025): 2543–2594, https://doi.org/10.1039/D4CS00845F.

6. S. Liu, L. Kang, and S. C. Jun, "Challenges and Strategies Toward Cathode Materials for Rechargeable Potassium-Ion Batteries," *Advanced Materials* 33 (2021): 2004689, https://doi.org/10.1002/adma.202004689.

7. Y. S. Xu, S. J. Guo, X. S. Tao, et al., "High-Performance Cathode Materials for Potassium-Ion Batteries: Structural Design and Electrochemical Properties," *Advanced Materials* 33 (2021): 2100409, https://doi.org/10.1002/adma.202100409.

8. R. Rajagopalan, Y. Tang, X. Ji, C. Jia, and H. Wang, "Advancements and Challenges in Potassium Ion Batteries: A Comprehensive Review," *Advanced Functional Materials* 30 (2020): 1909486, https://doi.org/10.1002/adfm.201909486.

9. X. Wang, Z. Xiao, K. Han, et al., "Advances in Fine Structure Optimizations of Layered Transition-Metal Oxide Cathodes for Potassium-Ion Batteries," *Advanced Energy Materials* 13 (2023): 2202861, https://doi.org/10.1002/aenm.202202861.

10. B. Zhang, Y. Choi, Z. Zhu, S. Zhao, and S. Guo, "Manganese-Based Layered Oxide Cathodes for Potassium-Ion Batteries: Progress and Outlook," *Advanced Energy Materials* (2025): 2501657, https://doi.org/10.1002/aenm.202501657.

11. Z. Caixiang, J. Hao, J. Zhou, X. Yu, and B. Lu, "Interlayer-Engineering and Surface-Substituting Manganese-Based Self-Evolution for High-Performance Potassium Cathode," *Advanced Energy Materials* 13 (2023): 2203126, https://doi.org/10.1002/aenm.202203126.

12. J. Liao, Y. Han, Z. Zhang, J. Xu, J. Li, and X. Zhou, "Recent Progress and Prospects of Layered Cathode Materials for Potassium-ion Batteries," *Energy & Environmental Materials* 4 (2021): 178–200, https://doi.org/10.1002/eem2.12166.

13. S. Chu, C. Shao, J. Tian, et al., "High Entropy-Induced Kinetics Improvement and Phase Transition Suppression in K-Ion Battery Layered Cathodes," *ACS Nano* 18 (2023): 337–346, https://doi.org/10.1021/acsnano.3c06393.

14. J. Vinckevičiūtė, M. D. Radin, and A. Van der Ven, "Stacking-Sequence Changes and Na Ordering in Layered Intercalation Materials," *Chemistry of Materials* 28 (2016): 8640–8650.

15. I. Dai, Y. Miyazaki, T. Kajitani, and K. Yubuta, "Experimental Verification of Quantized Conductance for Microwave Frequencies in Photonic Crystal Waveguides," *Physical Review B* 78 (2008): 184112, https://doi.org/10.1103/PhysRevB.78.073109.

16. H. Kim, J. C. Kim, S.-H. Bo, T. Shi, D.-H. Kwon, and G. Ceder, "K-Ion Batteries Based on a P2-Type $K_{0.6}$ CoO_2 Cathode," *Advanced Energy Materials* 7 (2017): 1700098, https://doi.org/10.1002/aenm.201700098.

17. H. Kim, D. H. Seo, J. C. Kim, et al., "Investigation of Potassium Storage in Layered P3-Type $K_{0.5}$ MnO_2 Cathode," *Advanced Materials* 29 (2017): 1702480, https://doi.org/10.1002/adma.201702480.

18. Y. Tang, H. Liu, X. Zhu, et al., "Restraining the Jahn–Teller Distortion in Mn-Based Layered Cathodes Toward High-Performance Potassium-Ion Batteries," *ACS Nano* 19 (2025): 21118–21129, https://doi.org/10.1021/acsnano.5c05389.

19. L. Yang, C. Shi, X. Pan, et al., "Activating Oxygen Redox in Layered K x TMO_2 to Construct High-Capacity and Enable Phase-Transition-Free Potassium Ion Cathode," *Advanced Functional Materials* 35 (2025): 2502974, https://doi.org/10.1002/adfm.202502974.

20. L. Liu, J. Liang, W. Wang, et al., "A P3-Type $K_{1/2}$ $Mn_{5/6}$ $Mg_{1/12}$ $Ni_{1/12}$ O_2 Cathode Material for Potassium-Ion Batteries With High Structural Reversibility Secured by the Mg–Ni Pinning Effect," *ACS Applied Materials & Interfaces* 13 (2021): 28369–28377, https://doi.org/10.1021/acsami.1c07220.

21. T. Wu, K. Liu, H. Chen, et al., "Rearrangement of Sodium Ordering and its Effect on Physical Properties in the $NaxCoO_2$ system," *Physical Review B* 78 (2008): 115122, https://doi.org/10.1103/PhysRevB.78.115122.

22. Z. Chen, B. Radhakrishnan, I. H. Chu, Z. Wang, and S. P. Ong, "Effects of Transition-Metal Mixing on Na Ordering and Kinetics in Layered P_2 Oxides," *Physical Review Applied* 7 (2017): 064003.

23. G. J. Shu and F. C. Chou, "Sodium-Ion Diffusion and Ordering in Single-Crystal P_2-$NaxCoO_2$," *Physical Review B* 78 (2008): 052101, https://doi.org/10.1103/PhysRevB.78.052101.

24. Y. Wang, R. Xiao, Y. S. Hu, M. Avdeev, and L. Chen, "P2-$Na_{0.6}[Cr_{0.6}Ti_{0.4}]O_2$ Cation-Disordered Electrode for High-Rate Symmetric Rechargeable Sodium-Ion Batteries," *Nature Communications* 6 (2015): 6954, https://doi.org/10.1038/ncomms7954.

25. J. L. Kaufman and A. Van der Ven, "Ordering and Structural Transformations in Layered K x CrO_2 for K-Ion Batteries," *Chemistry of Materials* 32 (2020): 6392–6400, https://doi.org/10.1021/acs.chemmater.0c01460.

26. M. Y. Toriyama, J. L. Kaufman, and A. V. Ven, "Potassium Ordering and Structural Phase Stability in Layered K x CoO_2," *ACS Appl Energy Mater* 2 (2019): 2629–2636.

27. P.-F. Wang, H.-R. Yao, X.-Y. Liu, et al., "Na^+ /Vacancy Disordering Promises High-Rate Na-Ion Batteries," *Science Advances* 4 (2018): aar6018, https://doi.org/10.1126/sciadv.aar6018.

28. Z. Xiao, J. Meng, F. Xia, et al., "K^+ Modulated K^+ /Vacancy Disordered Layered Oxide for High-Rate and High-Capacity Potassium-Ion Batteries," *Energy & Environmental Science* 13 (2020): 3129–3137, https://doi.org/10.1039/D0EE01607A.

29. S. M. Kang, J.-H. Park, A. Jin, Y. H. Jung, J. Mun, and Y.-E. Sung, "Na^+ /Vacancy Disordered P2-Na 0.67 Co 1– x Ti x O_2: High-Energy and High-Power Cathode Materials for Sodium Ion Batteries," *ACS Applied Materials & Interfaces* 10 (2018): 3562–3570, https://doi.org/10.1021/acsami.7b16077.

30. T. Yang, Y. Huang, J. Zhang, et al., "Insights Into Ti Doping for Stabilizing the $Na_{2/3}Fe_{1/3}Mn_{2/3}O_2$ Cathode in Sodium Ion Battery," *Journal of Energy Chemistry* 73 (2022): 542–548, https://doi.org/10.1016/j.jechem.2022.06.016.

31. T. Masese and G. M. Kanyolo, "Advancements in Cathode Materials for Potassium-Ion Batteries: Current Landscape, Obstacles, and Prospects," *Energy Advances* 3 (2024): 60–107, https://doi.org/10.1039/D3YA00406F.

32. J. U. Choi, J. Kim, J.-Y. Hwang, J. H. Jo, Y.-K. Sun, and S.-T. Myung, "$K_{0.54}[Co_{0.5}Mn_{0.5}]O_2$: New Cathode With High Power Capability for Potassium-Ion Batteries," *Nano Energy* 61 (2019): 284–294, https://doi.org/10.1016/j.nanoen.2019.04.062.

33. Y. Hironaka, K. Kubota, and S. Komaba, "P2- and P3-K x CoO_2 as an Electrochemical Potassium Intercalation Host," *Chemical Communications* 53 (2017): 3693–3696, https://doi.org/10.1039/C7CC00806F.

34. X. Zhang, Y. Yang, X. Qu, et al., "Layered P2-Type $K_{0.44}$ $Ni_{0.22}$ $Mn_{0.78}$ O_2 as a High-Performance Cathode for Potassium-Ion Batteries," *Advanced Functional Materials* 29 (2019): 1905679, https://doi.org/10.1002/adfm.201905679.

35. L. Duan, C. Shao, J. Liao, et al., "A P2/P3 Biphasic Layered Oxide Composite as a High-Energy and Long-Cycle-Life Cathode for Potassium-Ion Batteries," *Angewandte Chemie International Edition* 63 (2024): 202400868, https://doi.org/10.1002/anie.202400868.

36. Y. Sun, S. Guo, and H. Zhou, "Adverse Effects of Interlayer-Gliding in Layered Transition-Metal Oxides on Electrochemical Sodium-Ion Storage," *Energy & Environmental Science* 12 (2019): 825–840, https://doi.org/10.1039/C8EE01006D.

37. Z. Xiao, F. Xia, L. Xu, et al., "Suppressing the Jahn–Teller Effect in Mn-Based Layered Oxide Cathode Toward Long-Life Potassium-Ion

Batteries," *Advanced Functional Materials* 32 (2022): 2108244, https://doi.org/10.1002/adfm.202108244.

38. C. Liu, S. Luo, H. Huang, X. Liu, Y. Zhai, and Z. Wang, "Fe-Doped Layered P3-type $K_{0.45}Mn_{1-x}FexO_2$ ($x \leq 0.5$) as Cathode Materials for Low-Cost Potassium-Ion Batteries," *Chemical Engineering Journal* 378 (2019): 122167, https://doi.org/10.1016/j.cej.2019.122167.

39. Q. Zhang, C. Didier, W. K. Pang, et al., "Structural Insight Into Layer Gliding and Lattice Distortion in Layered Manganese Oxide Electrodes for Potassium-Ion Batteries," *Advanced Energy Materials* 9 (2019): 1900568, https://doi.org/10.1002/aenm.201900568.

40. Z. Xiao, J. Meng, Q. Li, et al., "Novel MOF Shell-Derived Surface Modification of Li-Rich Layered Oxide Cathode for Enhanced Lithium Storage," *Science Bulletin* 63 (2018): 46–53, https://doi.org/10.1016/j.scib.2017.12.011.

41. Y.-S. Xu, Y.-N. Zhou, Q.-H. Zhang, et al., "Layered Oxides With Solid-Solution Reaction for High Voltage Potassium-Ion Batteries Cathode," *Chemical Engineering Journal* 412 (2021): 128735, https://doi.org/10.1016/j.cej.2021.128735.

Supporting Information

Additional supporting information can be found online in the Supporting Information section.

Supporting File: adfm74473-sup-0001-SuppMat.docx.